MNRAS 000, 1–16 (2020) Preprint 5 March 2020 Compiled using MNRAS LaTeX style file v3.0

Cosmology dependency of halo masses and concentrations in hydrodynamic simulations

Antonio Ragagnin[1,2], Alexandro Saro[1,2,3], Priyanka Singh[1,2], Klaus Dolag[4,5]
[1] INAF-Osservatorio Astronomico di Trieste, via G.B. Tiepolo 11, 34143 Trieste, Italy
[2] IFPU - Institute for Fundamental Physics of the Universe, Via Beirut 2, 34014 Trieste, Italy
[3] Astronomy Unit, Department of Physics, University of Trieste, via Tiepolo 11, I-34131 Trieste, Italy
[4] University Observatory Munich, Scheinerstr 1, D-81679 Munich, Germany
[5] Max-Planck-Institut für Astrophysik (MPA), Karl-Schwarzschild Strasse 1, 85748 Garching bei München, Germany

5 March 2020

ABSTRACT
We employ a set of Magneticum cosmological hydrodynamic simulations that span over 15 different cosmologies, and extract masses and concentrations of all well-resolved haloes between $z = 0 - 1$ for critical over-densities $\Delta_{\mathtt{vir}}, \Delta_{200c}, \Delta_{500c}, \Delta_{2500c}$ and mean overdensity Δ_{200m}. We first show how a full physics description produce haloes 10%−20% less concentrated than non-radiative runs, which motivates us to provide the first fit of halo mass-concentration (Mc) of hydrodynamic simulations that is modelled by redshift and cosmological parameters $\Omega_m, \Omega_b, \sigma_8$ and h_0. We then investigate the possibility of converting masses from an overdensity $M_{\Delta 1}$ to an overdensity $M_{\Delta 2}$ with the aid of our mass-concentration relation and with a direct fit between mass values, namely a $M_{\Delta 1} - M_{\Delta 2}$ relation that is free from assumptions on the halo density profile. We study the uncertainty in the conversion of M_{2500c} and M_{500c} to M_{200c}, and find that converting M_{500c} to M_{200c} reaches the intrinsic fractional scatter of the mass-mass relationship (≈ 0.11), albeit there is a small fractional scatter (≈ 0.05) coming from non-NFWness of halo density profiles, while the conversion from M_{2500c} to M_{200c} strongly depends on the goodness of the mass-concentration fit. We show how a direct fit between mass values is a much precise tool for this kind of conversions. We release the package `hydro_mc` (github.com/aragagnin/hydro_mc), a python tool to use all kind of conversions presented in this paper.

Key words: concentration - haloes - numerical simulations

1 INTRODUCTION

Early studies of numerical simulations of cosmic structures embedded in cosmological volumes (see e.g. Navarro et al. 1997; Kravtsov et al. 1997) showed that dark matter haloes can be described by the so called Navarro Frank and White (NFW) profile (Navarro et al. 1996). The NFW density profile $\rho(r)$ is modelled by a characteristic density ρ_0 and a scale radius r_s in the following way:

$$\rho(r) = \frac{\rho_0}{\frac{r}{r_s}\left(1 + \frac{r}{r_s}\right)^2}. \quad (1)$$

The NFW profile proved to match density profiles of dark matter haloes of dark-matter-only simulations (see e.g. Bullock et al. 2001; Suto 2003; Prada et al. 2012; Meneghetti et al. 2014; Klypin et al. 2016; Gupta et al. 2017; Brainerd 2019) up to the most large and resolved ones whose analyses traces the route for the next generation of (pre-)Exascale simulations. Density profiles of hydrodynamic simulations have small deviations from the NFW profile (see e.g. Balmès et al. 2014; Tollet et al. 2016).

Since this kind of density profile does not have a cut-off radius, the radius of a halo is often chosen as the virial radius R_{vir} (see e.g. Ghigna et al. 1998; Frenk et al. 1999). Namely, the radius at which the mean density crosses the one of a theoretical virialised homogeneous top-hat overdensity. For a given cosmology, with a good approximation the virial overdensity can be written as

$$\Delta_{\mathtt{vir}}(a) \approx 18\pi^2 + 82 \cdot \Omega(a) - 39 \cdot \Omega(a), \quad (2)$$

where a is the scale factor and $\Omega(a)$ is the energy density parameter (see Dodelson 2003, for a review), namely

$$\Omega(a) = \Omega_m \cdot a^3 \cdot \left(\frac{\Omega_m}{a^3} + \frac{\Omega_r}{a^4} + \frac{\Omega_k}{a^2} + \Omega_\Lambda\right)^{-1}, \quad (3)$$

where $\Omega_m, \Omega_r, \Omega_k$ and Ω_Λ are the density fraction of respectively the total matter, radiation, curvature and cosmological constant. Numerical cosmological simulations, as in this work, typically uses negligible radiation and curvature terms (they set $\Omega_r = \Omega_k = 0$ in Eq. 3).

Observational studies typically define cluster radii $R_{\Delta c}$, where δ is an arbitrary overdensity and the "c" suffix indicates that the overdensity is relative to the critical overdensity, namely

$$M(r < R_{\Delta c}) = \frac{4}{3}\pi R^3_{\Delta c} \cdot \Delta \cdot \rho_c. \quad (4)$$

X-ray observations typically use overdensities Δ_{500c} and Δ_{2500c}, and the corresponding radii R_{500c} and R_{2500c} (the mean density crosses respectively $500\rho_c$ and $2500\rho_c$), see e.g. Bocquet et al. (2019); Umetsu et al. (2019); Mantz (2019); Bulbul et al. (2019). Observational studies that compute dynamical masses typically use $\Delta = \Delta_{200c}$ (see e.g. Biviano et al. 2017; Capasso et al. 2019). Weak Lensing studies on the other hand often utilise radii whose overdensities are proportional to the mean density of the Universe. For instance, works as Mandelbaum et al. (2008); McClintock et al. (2019) measure halo radii as R_{200m}, where the suffix "m" means that the radius is defined so the mean density in Eq. 4 of the halo crosses $\Delta\overline{\rho}$, (in this case $200\overline{\rho}$) where $\overline{\rho}$ is the average density of the Universe.

The concentration c_Δ of a halo is defined as

$$c_\Delta \equiv R_\Delta / r_s, \quad (5)$$

where r_s is the scale radius of Eq. 1 and scales quantifies how broad is the internal region of the cluster compared to its radius, for a given overdensity (see Okoli 2017, for a review).

Both numerical and observational studies analyse the concentration of haloes in the context of the so called mass-concentration (Mc) plane (see Table 4 in Ragagnin et al. 2019, for comprehensive list of recent studies).

Concentration parameter in both observational and numerical studies is found to have a weak dependence on halo mass and a very large scatter (Bullock et al. 2001; Martinsson et al. 2013; Ludlow et al. 2014; Shan et al. 2017; Shirasaki et al. 2018; Ragagnin et al. 2019).

The fractional scatter in the Mc plane can reach up to $\approx 33\%$ (Heitmann et al. 2016), and observations found outliers with an extremely high concentration. An example is the halo presented in Buote & Barth (2019), which has a concentration $3-6$ standard deviations above the median.

Part of the high scatter in the Mc relation is supposed to be due to different formation time of haloes with the same mass (Bullock et al. 2001; Rey et al. 2018), their different accretion history (see e.g. Fujita et al. 2018a,b) and due to the environment they are embedded in (Corsini et al. 2018; Klypin et al. 2016; Ragagnin et al. 2019)

The introduction of basic gas physics in cosmological simulations was found to increase halo concentration (Lin et al. 2006), while the additional description of radiative cooling processes does decrease it (Duffy et al. 2010). An additional factor that decreases the concentration is the effect of Active Galactic Nuclei (AGN) feedback (Duffy et al. 2010). When all major physical phenomena of galaxy formation are taken into account (cooling, star formation, black hole seeding and their feedback), then concentration parameters are lower than their dark-matter-only counterpart (see e.g. results from NIHAO simulations as in Wang et al. 2015; Tollet et al. 2016).

Different cosmological models (see e.g. Roos 2003, for a review on cosmological models) also produce Mc relations with different behaviours: switching from Cold Dark Matter (CDM) to ΛCDM (Kravtsov et al. 1997) produce less massive and more concentrated haloes; while dark energy models with a equation of state having $w > -1.0$ produce haloes with lower concentrations than in ΛCDM (Dolag et al. 2004; De Boni 2013; De Boni et al. 2013).

Another important study on the dependency of concentration from cosmological model is given by the Cosmic Emulator (Bhattacharya et al. 2013; Heitmann et al. 2016). Cosmic Emulator extensively studies the dependency of the concentration as a function of different cosmologies (in the context of wCDM cosmologies) for dark matter only simulations.

Macciò et al. (2008) investigate the effects on concentration of haloes in dark matter only simulations using cosmological parameters of various Wilkinson Microwave Anisotropy Probe (WMAP) releases (Spergel et al. 2003, 2007; Komatsu et al. 2009). They see an overall increase of halo concentrations when switching from WMAP1 to WMAP2 and to WMAP3, although it is difficult to infer the effect that each cosmological parameter change has in the mass-concentration plane.

Prada et al. (2012) show how the dependence of concentration on mass and redshift can be obtained from the root mean square fluctuation amplitude of the linear density field $\sigma(M, z)$, and show that the $\sigma - c$ relation has less scatter than the Mc relation, with a nearly-universal simple U-shaped behaviour and a minimum near $\sigma \approx 0.71$.

Some theoretical works of dark matter only simulations find an up turn at the very high mass regime of the Mc plane (Klypin et al. 2011). This puzzling behaviour has been found to be consequence of their high σ (making NFW a bad fit formula) value of these haloes and is in agreement with the $\sigma - c$ relation Diemer & Kravtsov (2015); Diemer & Joyce (2019). More generally, Balmès et al. (2014) show that haloes that are ill-described by a NFW profile have lower concentration than average (see Figure 5 in their paper).

The mass-concentration plane is an important tool to test cosmological models (Kendall & Easther 2019) and to convert masses between two over-densities. For this purpose Balmès et al. (2014) define the so called sparsity parameter $s_{\Delta 1, \Delta 2}$, as the ratio between masses at over-density Δ_1 and Δ_2. This quantity is a proxy to the total matter profile (Corasaniti et al. 2018), and enables cosmological parameter inference (Corasaniti & Rasera 2019) and to test for some dark energy models without assuming an NFW profile (Balmès et al. 2014). Observations uses the sparsity parameter to infer the halo matter profile (Bartalucci et al. 2019), as a potential probe to test $f(R)$ models (Achitouv et al. 2016), a less uncertain measurement of the mass-concentration relation (Fujita et al. 2019), and to find outlier in scaling relations involving integrated quantities with different radial dependencies (see conclusions in Andreon et al. 2019).

Although the concentration parameter was first introduced for haloes of dark-matter-only simulations, observations point to the direction that the total matter density profile (which includes baryons) is typically approximated by a NFW profile as well (Biviano & Girardi 2003; Becker

& Kravtsov 2011; Biviano et al. 2013; Mamon et al. 2013; Capasso et al. 2019). For this reason in this work we will fit the NFW profile to the total matter profile (i.e. including dark matter, gas and star component).

In this work we study the concentration of haloes of the Magneticum[1] suite of hydrodynamic cosmological simulations (Dolag et al. 2015, 2016), and model the Mc plane as a function of cosmology. Additionally this work test the possibility of converting masses between two over-densities and taking into account the dependency on cosmological parameters, with and without the aid of a Mc relation.

The plan of this paper is as follows. In Section 2 we present the numerical set up of the simulations used in this work. In Section 3 we fit the concentration of haloes as a function of mass and scale factor for all our simulations and compare our results with both observations and other theoretical studies. In Section 4 we provide a fit of the concentration as a function of mass, scale factor and cosmology. In Section 5 we test the possibility of converting masses from one overdensity to another overdensity, by using the Mc fit or a direct mass-mass (M-M) fit. We draw our conclusions in Section 6.

2 NUMERICAL SIMULATIONS

The Magneticum simulations (presented in works as Biffi et al. 2013; Saro et al. 2014; Steinborn et al. 2015; Dolag et al. 2016, 2015; Teklu et al. 2015; Steinborn et al. 2016; Bocquet et al. 2016; Remus et al. 2017) are performed with an extended version of the N−body/SPH code P-Gadget3, which is the successor of the code P-Gadget2 (Springel et al. 2005b; Springel 2005; Boylan-Kolchin et al. 2009), with a space-filling curve aware neighbour search (Ragagnin et al. 2016), an improved Smoothed Particle Hydrodynamics (SPH) hydrodynamics solver Beck et al. (2016); treatment of radiative cooling, heating, ultraviolet (UV) back-ground, star formation and stellar feedback processes as in Springel et al. (2005a) connected to a detailed chemical evolution and enrichment model as in Tornatore et al. (2007), which follows 11 chemical elements (H, He, C, N, O, Ne, Mg, Si, S, Ca, Fe) with the aid of CLOUDY photo-ionisation code (Ferland et al. 1998). Fabjan et al. (2010); Hirschmann et al. (2014) describe prescriptions for black hole growth and for feedback from AGNs.

Haloes are identified using a version of SUBFIND (Springel et al. 2001), adapted by Dolag et al. (2009) to take into account the baryon component.

The detailed description of baryon physics in Magneticum simulations is capable of matching several observed properties of galaxies and their haloes. For instance: the specific angular momentum for different morphologies (Teklu et al. 2015, 2016); the mass-size relation (Remus & Dolag 2016; Remus et al. 2017; van de Sande et al. 2019); the dark matter fraction (see Figure 3 in Remus et al. 2017); the baryon conversion efficiency (see Figure 10 in Steinborn et al. 2015); kinematical observations of early-type galaxies (Schulze et al. 2018); the inner slope of the total matter density profile (see Figure 7 in Bellstedt et al. 2018), the ellipticity and velocity over velocity dispersion ratio (van de Sande et al. 2019), and reproduce the high concentration of fossil objects (Ragagnin et al. 2019).

Table 1 shows an overview of the cosmological simulations used in this work. They have been already presented in Singh et al. (2019) (see Table 1 in their paper) and labelled as C1–15. Each simulation covers a volume of $896Mpc/h$ and have a different configuration of the cosmological parameter $\Omega_m, \Omega_b, h,$ and σ_8. Additionally two simulations with the same setup as C1 and C15 (C1_norad and C15_norad) have been run without radiative cooling and star formation.

For each simulations we study the haloes at a timeslice with redshifts $z = 0.00,\ 0.14,\ 0.29,\ 0.47,\ 0.67,$ and $z = 0.90$. In the following sections we repeat the same analyses for overdensities $\Delta_{\mathtt{vir}}, \Delta_{200c}, \Delta_{500c}, \Delta_{2500c}, \Delta_{200m}$ and for each overdensity we perform a mass-cut (respectively on $M = M_{\mathtt{vir}}, M_{200c}, M_{500c}, M_{2500c}, M_{200m}$) that ensures that all haloes have at least 10^4 particles. This cut is different for each of our simulations. This is opposed to what was used in Singh et al. (2019), where they choose a fixed mass cut for all C1-C15 simulations.

In this work we fit the NFW profile (see Eq. 1) over the *total matter component* (i.e. dark matter and baryons) as opposed to previous works (Ragagnin et al. 2019, see) where the NFW profile fit was performed over the dark matter component only. We fit the density profile over 20 logarithmic bins, starting from $r = 500kpc/h$ (similar to the cut in the observational studies as Dietrich et al. 2019). All fits with a $\chi^2 > 10^3$ have been excluded from our analyses (which accounts for few hundreds haloes per snapshot) as they correspond to objects undergoing major mergers.

3 HALO CONCENTRATIONS

In this section we study the importance of computing concentration in hydrodynamic simulations and compare Magneticum halo concentrations with other studies.

We first show the importance of correctly describe baryon physics, and how an incorrect description impact halo concentrations. Since all simulations share the same initial conditions, it is possible to look at the evolution of the same halo that evolved in different cosmologies.

Figure 1 shows the evolution of both the virial radii and scale radii of haloes in C1 and C1_norad. Figure 1 (upper panel) show the stacked ratio of concentration, virial radius and ascale radius. There we can see that on average C1 haloes have higher concentration parameters ($\approx 10-15\%$ higher, up to $\approx 20\%$) and this difference grows with time. On the other hand, the virial radius is similar between haloes of C1 and C1_norad. Scale radius lead the variation in concentration. Figure 1 (bottom panel) focus on the evolution of a single halo (bottom left panel shows C1 and bottom right panel shows the same halo in C1_norad). Simulations without radiative cooling produce haloes with lower concentration with respect to their full physics counter part (i.e. $c_{vir} \approx 6$ lowers down to $c_{vir} \approx 5$). This example shows that in non-radiative simulations, concentration decreases even if the full physics counter part is characterised by the same accretion history ("jumps" in concentration and r_s values happens at the same scale factor).

[1] http://www.magneticum.org

Table 1. List of Magneticum simulations as presented in Singh et al. (2019). Columns show, respectively: simulation name, cosmological parameters $\Omega_m, \Omega_b, \sigma_8$, and h_0, the number of haloes selected from all redshift snapshots ($z = 0.00,\ 0.14,\ 0.29,\ 0.47,\ 0.67,$ and $z = 0.90.$) of a given simulation and the number of haloes of that simulations at redshift $z = 0$. Two of these simulations were also run without radiative processes (C1_norad and C1_norad).

Name	Ω_m	Ω_b	σ_8	h_0	N_{haloes} (all snapshots)	N_{haloes} (snapshot $z=0$)	
C1	0.153	0.0408	0.614	0.666	29206	9153	
C1_norad	0.153	0.0408	0.614	0.666	27613	9208	no radiative processes
C2	0.189	0.0455	0.697	0.703	54094	16236	
C3	0.200	0.0415	0.850	0.730	107423	27225	
C4	0.204	0.0437	0.739	0.689	66351	19051	
C5	0.222	0.0421	0.793	0.676	84087	22037	
C6	0.232	0.0413	0.687	0.670	47045	14930	
C7	0.268	0.0449	0.721	0.699	58815	17990	
C8	0.272	0.0456	0.809	0.704	79417	22353	Komatsu et al. (2011) cosmology
C9	0.301	0.0460	0.824	0.707	96151	26473	
C10	0.304	0.0504	0.886	0.740	120617	32551	
C11	0.342	0.0462	0.834	0.708	97392	27100	
C12	0.363	0.0490	0.884	0.729	118342	33571	
C13	0.400	0.0485	0.650	0.675	35503	14626	
C14	0.406	0.0466	0.867	0.712	104266	30918	
C15	0.428	0.0492	0.830	0.732	92352	28348	
C15_norad	0.428	0.0492	0.830	0.732	79399	25270	no radiative processes

3.1 Redshift-mass-concentration plane

We perform a fit of the concentration as a function of mass and redshift for each simulation and each over-density Δ. The functional form of the concentration is chosen as a power law on mass and scale factor as done in some observational works (see e.g. Merten et al. 2015) as:

$$\ln\, c_\Delta\left(M_\Delta\right) = \ln A + B \ln\left(\frac{M_\Delta}{M_p}\right) + C \ln\left(\frac{a}{a_p}\right) + \sigma, \qquad (6)$$

here A, B are fit parameters and a, M_p are median of mass and scale factor and are used as pivot values, σ is the logarithmic scatter.

We maximised the following likelihood $\hat{\mathcal{L}}$[2] with a uniform prior for all fit parameters:

$$\ln\, \hat{\mathcal{L}} = -\frac{1}{2}\left(\ln(2\pi\sigma^2) + \left(\frac{\ln\, c_{fit} - \ln\, c_\Delta}{\sigma}\right)^2\right). \qquad (7)$$

Figure 2 shows the mass concentration planes for $\Delta_{\mathtt{vir}}$ (computed following Eq. 2) for all 15 simulations, together with the concentration from the redshift-mass-concentration (aMc relation) colour coded by $log_{10}\chi^2$. Here we can see that haloes with low χ^2 tend to have lower concentration. This qualitatively agrees with other theoretical studies that show how perturbed objects have lower concentrations (see e.g. Balmès et al. 2014; Ludlow et al. 2014; Klypin et al. 2016). For this reason, in a mass-concentration plane it is not advisable to weight halo concentrations with χ^2, as this would add a bias the relation towards higher concentrations. Although the dependency of concentration from halo mass is believed to decrease, extreme cosmologies such as C1 and C2 (they have $\Omega_m < 0.2$) have an over all positive dependency between mass and concentration. On the other hand, the logarithmic mean slope low (between -0.03 and 0.08) and its influence in the mass concentration plane is not dominant in our mass regime.

3.2 Comparison with other studies

The average concentrations of haloes shown in Figure 4 are higher than the concentration computed over the dark-matter density profile presented in a previous work on Magneticum simulations (Ragagnin et al. 2019, which uses the same cosmology as C8). The median concentration for cosmology C8 is $c_{200c} \approx 3.50$ for the total matter profile, while the dark matter concentration presented in (Ragagnin et al. 2019) has $c_{200c} \approx 4.3$.

Such discrepancy is due to the fact that dark matter component is more peaked in the central region with respect to the total matter density. Figure 3 shows an example of the matter density profiles of a Magneticum halo, this example points to the importance of presence of baryon physics in cosmological simulations.

We then compare Magneticum simulations concentrations of haloes with the concentration predicted by the Cosmic Emulator (Heitmann et al. 2016; Bhattacharya et al. 2013). The Cosmic Emulator predicts the mass-concentration planes for a given $wCDM$ cosmology (to match their cosmology with ours we used a value of $w = -1$).

The ratio of median concentration $c_{\mathtt{vir}}$ parameters of haloes obtained with our mass-concentration fit and the concentration provided by the Cosmic Emulator (Heitmann et al. 2016; Bhattacharya et al. 2013) for each of our simulation whose cosmology (C7, C8 and C9 only) is ≈ 1.2.

We were able to compare only C7, C8 and C9 cosmology because the other Magneticum simulations had cosmological parameters that were out of the range of the Cosmic Emulator. We notice how the Cosmic Emulator concentrations

[2] we used the `python` package `emcee` (Foreman-Mackey et al. 2013)

Figure 1. Evolution of virial and scale radii and concentration of haloes in simulations C1 and C1_norad. Upper panel shows the stacked average over 50 haloes of ratios of $c_{\mathtt{vir}}, R_{\mathtt{vir}}$ and r_s. between the same haloes in C1 and C1_norad. Lower panel show the evolution of a single halo in the simulation C1 with full physics of, respectively $R_{\mathtt{vir}}$ (in blue) and r_s (in orange) and $c_{\mathtt{vir}}$ in blue, as described in Section 2 (bottom left plots) versus non-radiative runs (bottom right plots).

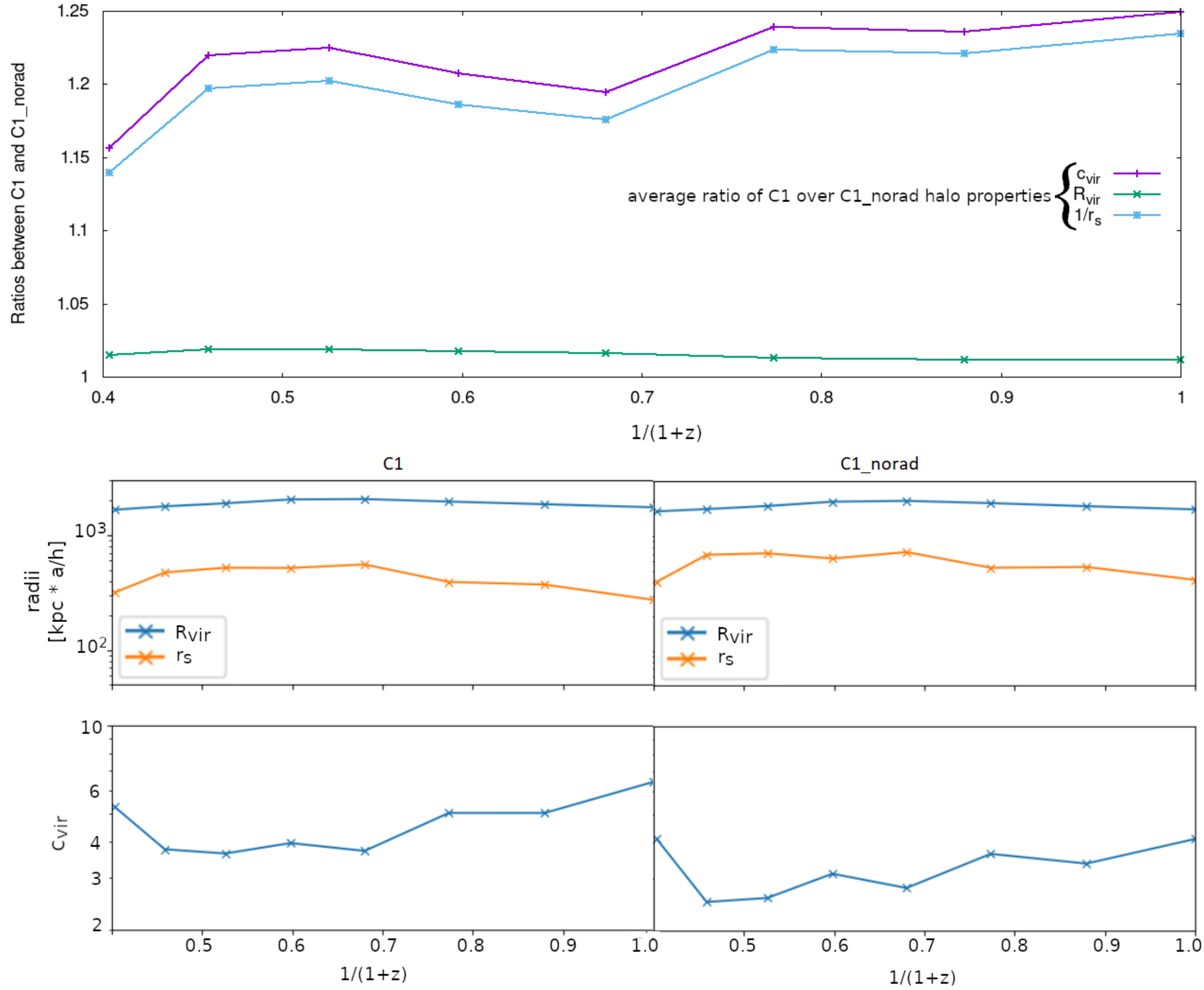

(retrieved by dark matter only runs) is systematically higher than Magneticum simulations in this mass regime (by a factor of $\approx 10-20\%$), in agreement with our comparison in Ragagnin et al. (2019).

The scatter is constant over mass, redshift and cosmology, to nearly $\sigma \approx 0.38$, in agreement with the value of $\approx 1/3$ presented in the $wCDM$ dark-matter only model of Kwan et al. (2013).

Figure 4 shows the mass-concentration plane for the full-physics simulations C1–15 against other dark matter only simulations and observations. We compare against concentration of Omega500 simulations (Shirasaki et al. 2018); CLASH concentrations from Merten et al. (2015), numerical predictions from MUSIC of CLASH (Meneghetti et al. 2014) where a number of simulated haloes have been chosen to make mock observations for CLASH; and fossil groups from Pratt et al. (2016). When analysing this data one must be aware of their selection effects: CLASH data set underwent some filtering difficult to model, while fossil objects presented in Pratt et al. (2016) by construction lay in the upper part of the Mc plane. There is a general match between concentration of Magneticum simulations and observations.

4 COSMOLOGY DEPENDENCE OF CONCENTRATION PARAMETER

The 15 cosmologies we use in this work have different mass-concentration normalisation values and log-slope (see Figure 2). we perform a fit of the concentration as a function of mass, scale factor and cosmological parameters in order to interpolate a mass-concentration plane at a given, arbitrary, cosmology. Namely concentration $c_\Delta\left(M_\Delta, 1/\left(1+z\right), \Omega_m, \Omega_b, \sigma_8, h_0\right)$. As the intrinsic scat-

Figure 2. Each panel shows the mass-concentration plane one full physics Magneticum simulation presented in Table 1. Concentrations are computed at overdensity Δ_{vir}. Points represents a all selected haloes at redshift $z = 0$, colour-coded by their $log_{10}\chi^2$. Concentration values are plotted only in the range $c_{\texttt{vir}} = 1 - 10$, because this range contains vast majority of haloes. Black line corresponds to the mass-concentration relation obtained by the fit in Eq. 6. Gray lines corresponds to the mass-concentration relation obtained for the simulation C8 (which uses the reference cosmology Komatsu et al. (2009)). The different mass-cut on each panel is due to our choice of selecting the smallest mass-cut where all haloes with at least 10^4 particles. As a consequence, our mass-cuts depend on cosmological parameters.

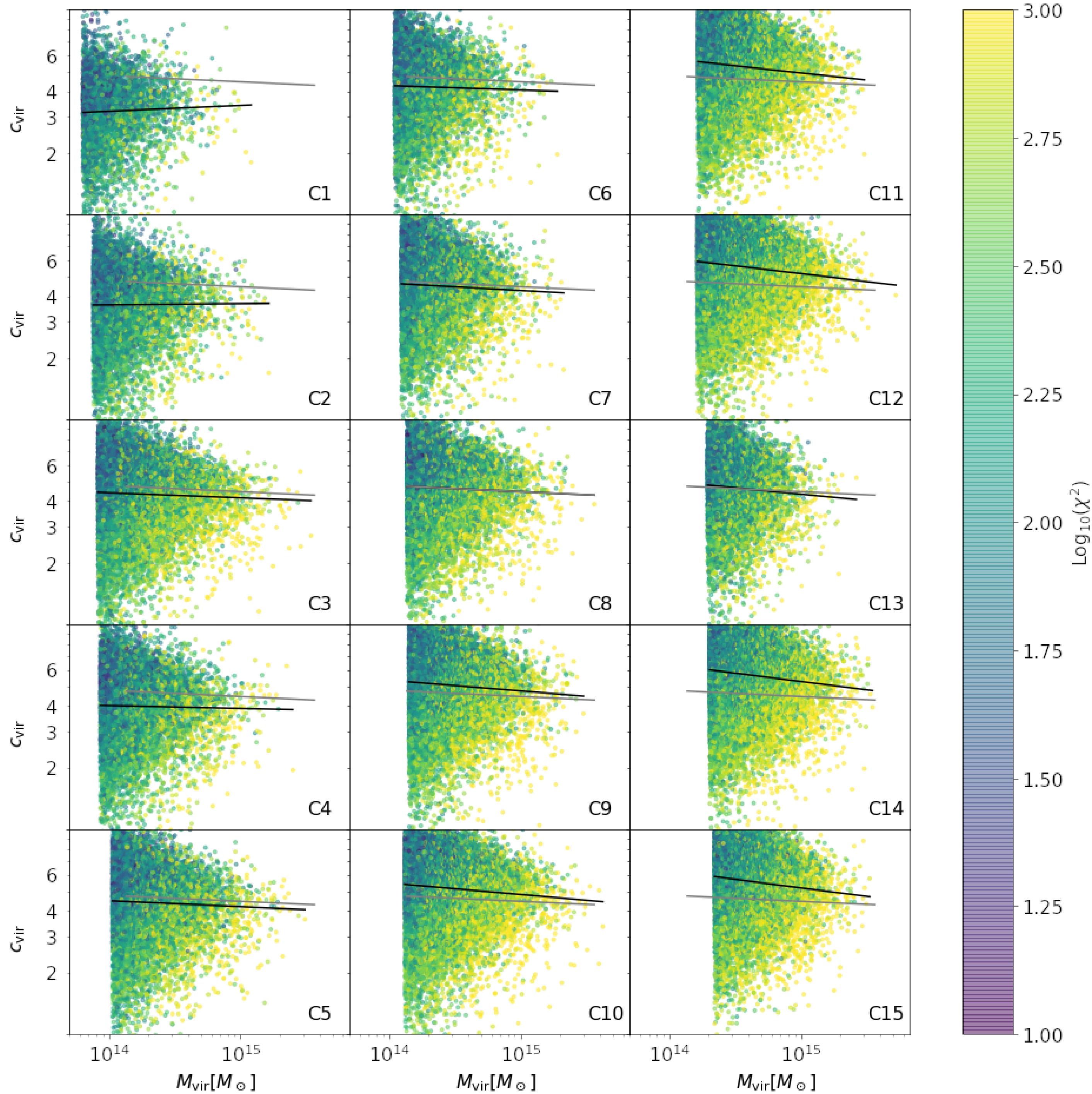

Figure 3. Density profile of both dark matter (dashed black) and total matter (dashed pink) up to the virial radius $R_{\tt vir} = 930 kpc/h$ and the corresponding NFW profile (solid lines) for a halo of C1 simulation at $z = 0$. Vertical lines correspond respectively to the dark matter profile scale radius ($139 kpc/h$) and the total matter profile has a scale radius $r_s = 154 kpc/h$.

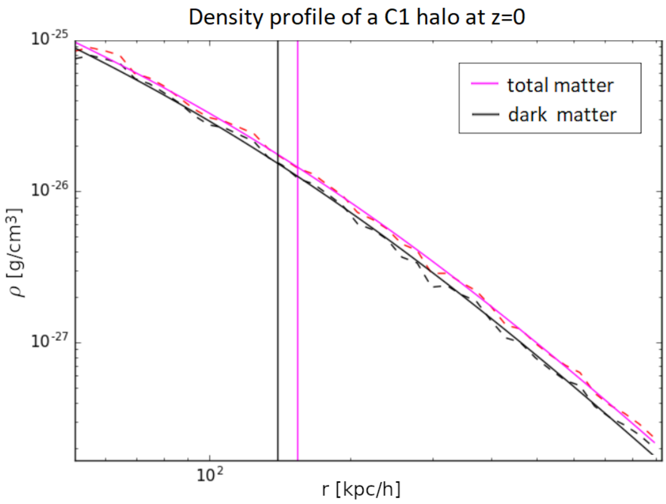

ter is constant (within few percents) we didn't further parametrised it in the fit and it is assumed to be independent from mass, redsjift and cosmology. The functional form of the fit parameters in Eq. 6, with a dependency on cosmology is as

follows:

$$\begin{aligned}
A = &\quad A_0 + \alpha_m \ln\left(\frac{\Omega_m}{\Omega_{m,p}}\right) + \alpha_b \ln\left(\frac{\Omega_b}{\Omega_{b,p}}\right) + \\
&\quad + \alpha_\sigma \ln\left(\frac{\sigma_8}{\sigma_{8,p}}\right) + \alpha_h \ln\left(\frac{h_0}{h_{0,p}}\right) \\
B = &\quad B_0 + \beta_m \ln\left(\frac{\Omega_m}{\Omega_{m,p}}\right) + \beta_b \ln\left(\frac{\Omega_b}{\Omega_{b,p}}\right) + \\
&\quad + \beta_\sigma \ln\left(\frac{\sigma_8}{\sigma_{8,p}}\right) + \beta_h \ln\left(\frac{h_0}{h_{0,p}}\right) \\
C = &\quad C_0 + \gamma_m \ln\left(\frac{\Omega_m}{\Omega_{m,p}}\right) + \gamma_b \ln\left(\frac{\Omega_b}{\Omega_{b,p}}\right) + \\
&\quad + \gamma_\sigma \ln\left(\frac{\sigma_8}{\sigma_{8,p}}\right) + \gamma_h \ln\left(\frac{h_0}{h_{0,p}}\right)
\end{aligned} \tag{8}$$

The fit has been performed for $\Delta = \Delta_{\tt vir}, \Delta_{200c}, \Delta_{500c}, \Delta_{2500c}$ and Δ_{200m} by maximising the Likelyhood as in Eq 7. Table 2 shows the results with pivots the reference cosmology of C8 (Komatsu et al. 2011). To evaluate systematic errors due to model assumptions, statistical errors are treated as in Singh et al. (2019): for each simulation we take its pivot values (as in Table 2) and fit all haloes of all simulations using Eq. 6 and 8, we then assign the standard deviation of parameters as fit errors in αs,βs and γs. We then use the fit parameters of the fit with the same pivots as C8 cosmology.

From this fit we can see how the normalisation (α parameters) is mainly affected by the Ω_m and σ_8 parameter.

The slope of the mass-concentration plane (β parameters) has a weak dependency from cosmology. On the other hand, we can still see how this is pushed towards a negative logarithmic slope by an increase in Ω_m and h_0 (because $\beta_m, \beta_h < 0$), while it is pushed towards a positive correlation by an increase in Ω_b and σ_8 (because $\beta_b, \beta_\sigma > 0$). This behaviour was already shown in Figure 4 C1 and C2 have a opposite mass-dependency (A parameter) with respect to the other runs. Although the trend can be positive for some cosmologies (see Table 2 and Figure 2), the slope is always close to zero.

The redshift dependency (γ parameters) is driven by both σ_8 and Ω_m, while a high baryon fraction can lower the dependency (see parameter γ_h)

The scatter is constant with all overdensities to nearly 0.38.

Given the weak dependency on cosmology from the logarithmic slope of the mass, Appendix A (see Table A1) shows a similar fit as the one of this section, where B in Eq. 8 has no dependency form the cosmology (i.e. $B = B_0$). In Appendix A (see Table A2) we also provide the same reduced fit parameters with the scale radius computed on the dark matter density profile.

5 HALO MASSES CONVERSION

In the following subsections we study the possibility of converting masses from one overdensity to the other (e.g. the problem of obtaining M_{200} given M_{500}).

To study the origin of the scatter coming from this kind of conversion we also provide a direct fit for converting masses (i.e. SUBFIND masses) from $\Delta 1$ to $\Delta 2$, thus without using the Mc relation. This kind of conversions is used in computing the sparsity of haloes (i.e. ratio of masses in two overdensities), which itself can probe cosmological parameters (Corasaniti et al. 2018; Corasaniti & Rasera 2019) and dark energy models (Balmès et al. 2014).

5.1 Mass-mass conversion using Mc relation

Here we study in detail how to convert masses values from two overdensities using the Mc relation. By combining the definition of mass M_Δ (see Eq. 4) and the fact that the matter profile only depends on a proportional parameter ρ_0 and a scale radius r_s, we get

$$M_\Delta = 4\pi\rho_0 r_s^3 f(c_\Delta) = \Delta \frac{4}{3}\pi R_\Delta^3 \rho_c, \tag{9}$$

For a NFW profile as in Eq. 1 it holds that

$$f(c_\Delta) = \quad \ln(1 + c_\Delta) - \frac{c_\Delta}{1 + c_\Delta}. \tag{10}$$

Combining Eq. 9 and 10 gives the following mass conversion formula:

$$\begin{cases} M_{\Delta 2} = M_{\Delta 1}\left(\dfrac{c_{\Delta 2}}{c_{\Delta 1}}\right)^3 \dfrac{\Delta_2}{\Delta_1} \\ \\ c_{\Delta,2} = c_{\Delta,1} \cdot \left(\dfrac{\Delta_1}{\Delta_2}\dfrac{f(c_{\Delta,2})}{f(c_{\Delta,1})}\right)^{\frac{1}{3}}. \end{cases} \tag{11}$$

Figure 4. Mass concentration plane of our simulations C1-C15, and other studies in the literature. Shaded area shows the best relation and its intrinsic scatter (within one sigma) for the reference cosmology C8. We compare with the mass-concentration plane of Omega500 (Shirasaki et al. 2018), and observations of fossil groups from Pratt et al. (2016), mock observations from Meneghetti et al. (2014) and data from CLASH (Merten et al. 2015).

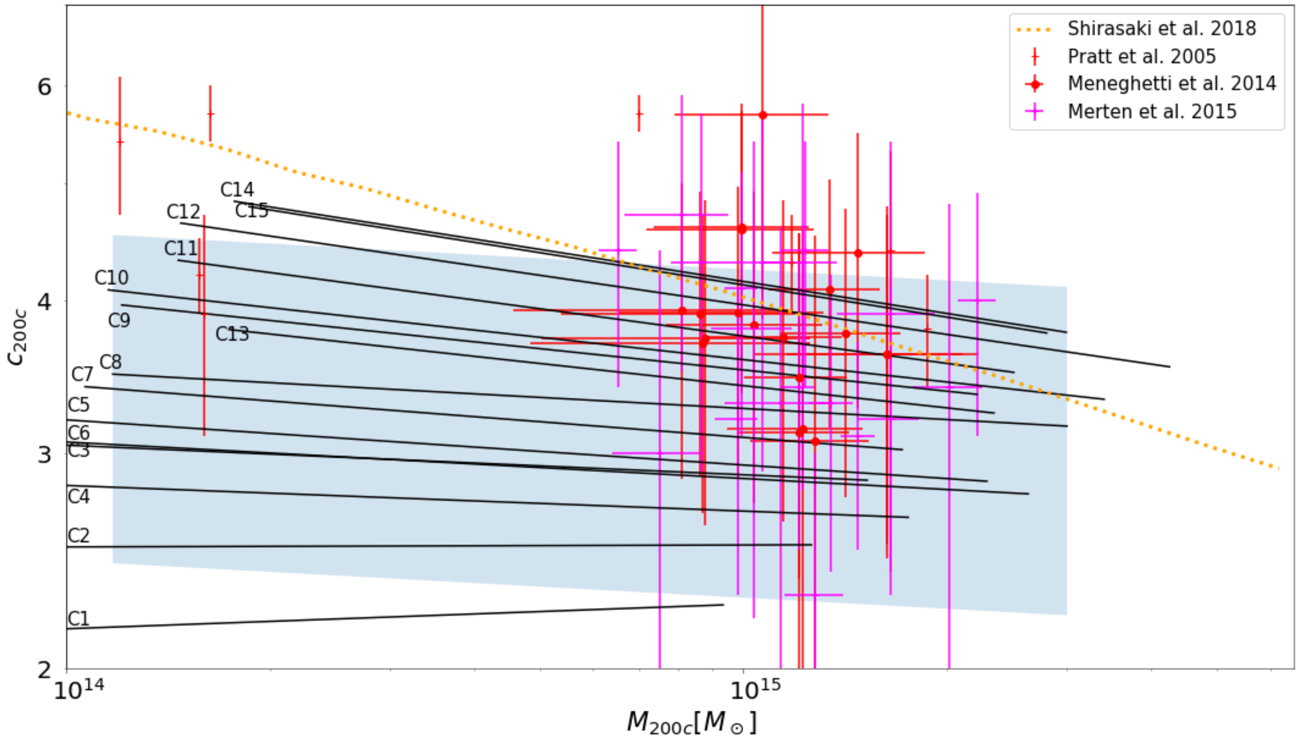

Table 2. Pivots and best fit parameters for the cosmology-redshift-mass-concentration plane and its dependency on cosmology as in Eq. 6 and Eq. 8 for concentration overdensities of $\Delta = \Delta_{\texttt{vir}}, \Delta_{200c}, \Delta_{500c}, \Delta_{2500c}$ and Δ_{200m}. The pivots $\Omega_{m,p}, \Omega_{b,p}, \sigma_8$ and h_0 in Eq. 8 are the cosmological parameters of C8 as in Table 1 ($\Omega_m = 0.272, \Omega_b = 0.0456, \sigma_8 = 0.809, h_0 = 0.704$). Pivots a_p and M_p are respectively median of scale factor an mass of all haloes. Errors on A_0, B_0, C_0 and σ are omitted as they are all $< 0.001\%$. The package `hydro_mc` contains a script that utilises this relation (`http://github.com/aragagnin/hydro_mc/blob/master/examples/sample_mc.py`).

Param	Overdensity				
	vir	200c	500c	2500c	200m
$M_p[M_\odot]$	$1.99e+14$	$1.74e+14$	$1.37e+14$	$6.87e+13$	$2.24e+14$
a_p	0.877	0.877	0.877	0.877	0.877
A_0	1.503	1.244	0.864	0.127	1.692
B_0	-0.043	-0.048	-0.053	-0.031	-0.040
C_0	0.516	0.204	0.188	0.107	0.909
α_m	0.45 ± 0.04	0.63 ± 0.04	0.66 ± 0.04	0.76 ± 0.05	0.23 ± 0.04
α_b	-0.25 ± 0.04	-0.25 ± 0.04	-0.23 ± 0.05	-0.3 ± 0.1	-0.27 ± 0.03
α_σ	0.55 ± 0.03	0.56 ± 0.03	0.52 ± 0.05	0.42 ± 0.05	0.53 ± 0.02
α_h	-0.00 ± 0.03	-0.03 ± 0.02	-0.03 ± 0.07	-0.0 ± 0.2	0.02 ± 0.03
β_m	-0.1220 ± 0.0008	-0.1178 ± 0.0005	-0.1124 ± 0.0009	-0.116 ± 0.001	-0.116 ± 0.001
β_b	0.117 ± 0.005	0.112 ± 0.004	0.126 ± 0.005	0.289 ± 0.007	0.115 ± 0.008
β_σ	0.051 ± 0.003	0.056 ± 0.002	0.088 ± 0.004	0.103 ± 0.005	0.050 ± 0.006
β_h	-0.08 ± 0.01	-0.044 ± 0.009	-0.16 ± 0.01	-0.34 ± 0.02	-0.09 ± 0.03
γ_m	0.240 ± 0.006	0.352 ± 0.007	0.346 ± 0.009	0.38 ± 0.01	-0.043 ± 0.009
γ_b	-0.13 ± 0.03	-0.04 ± 0.04	-0.04 ± 0.05	-0.13 ± 0.06	-0.06 ± 0.05
γ_σ	0.66 ± 0.03	0.77 ± 0.03	0.86 ± 0.03	0.85 ± 0.05	0.64 ± 0.04
γ_h	-0.0 ± 0.1	-0.3 ± 0.1	-0.3 ± 0.1	0.0 ± 0.2	-0.4 ± 0.1
σ	0.387796	0.384312	0.376513	0.382735	0.388255

From bottom Eq. 11 it is possible to evaluate the concentration $c_{\Delta 2}$ as a function of only $c_{\Delta 1}$ (as in Appendix C of Hu & Kravtsov 2003).

Eq. 11 can be used to estimate the theoretical scatter σ_{theo} obtained in the mass conversion by analytically propagating the uncertainties of the mass-concentration relation, namely:

$$\sigma_{theo} = \frac{1}{M_{\Delta 2}} \frac{dM_{\Delta 2}}{dc_{\Delta 1}} \sigma_{c,\Delta 1}, \tag{12}$$

where $M_{\Delta 2}$ is the converted mass, $c_{\Delta 1}$ the concentration in the original overdensity Δ_1 and $\sigma_{c,\Delta 1}$ is the uncertainty in the concentration values (in our case it is the scatter in the Mc relation). Appendix B describes how to obtain the theoretical scatter one would expect given perfectly NFW profiles.

One would expect that the mass-mass conversion derived by a mass-concentration relation, has several sources of error: (i) the intrinsic scatter of the Mc relation (σ_{Mc}) that must be propagated to σ_{theo}, (ii) the fact that profiles are not perfectly NFW and thus Eq. 10 is not the best choice for this conversion; (iii) the cosmology-redshift-mass-concentration fit (as in Table 2) is not optimal.

To further study the sources of uncertainties in this conversion, we will fit halo masses between two overdensities[3], and compare the two conversion methods together.

5.2 $M_{\Delta 1}$-$M_{\Delta 2}$ (M-M) plane

To study the uncertainty obtained converting masses passing through an Mc relation, and to also provide a way of converting masses without any assumption on their concentration and NFW density profile, we perform a direct fit between halo masses (i.e. SUBFIND masses), as a function of redshift and cosmological parameter. For each pair of overdensities we performed a fit of the mass $M_{\Delta 2}\left(M_{\Delta 1}, 1/\left(1+z\right), \Omega_m, \Omega_b, \sigma_8, h_0\right)$ with the following functional form:

$$\ln\ M_{\Delta 2}\left(M_{\Delta 1}, a\right) = \ln A + B \ln\left(\frac{M_{\Delta 1}}{M_p}\right) + C \ln\left(\frac{a}{a_p}\right) \tag{13}$$

where A, B, C parameters are parametrised with cosmology as in Eq. 8.

Table 3 show the results of the mass-mass conversion fit between critical overdensities, while Table 4 show the conversion fit parameters between Δ_{200c} and Δ_{200m}. We can see that this kind of relation has a strong dependency from σ_8 and a weak dependency from h_0 (see $\alpha_m, \beta_m, \gamma_m$ parameters). We quantitatively discuss these results in the discussion Section 6.

5.3 Uncertainties in mass conversions

When converting between masses at different overdensities, we make use of the following uncertainties:

- the scatter σ_{M-M} from the mass-mass fit as Sec 5.2
- the scatter $\sigma_{M-M(Mc)}$ from the mass-mass conversion obtained with the aid of our Mc relation (as in Sec 5.1)
- in order to estimate the error coming from non-NFWness (i.e. deviation from perfect NFW density profile), we will compute the scatter $\sigma_{M-M(c)}$ obtained from a conversion between the true values of $M_{\Delta 1}$ and $c_{\Delta 1}$ of a given halo to the mass $M_{\Delta 2}$ (i.e. using only Eq. 11)
- the scatter σ_{theo} obtained by analytically propagating the Mc log-scatter (of approx. 0.38) with Eq. 12
- the hypothetical scatter $\tilde{\sigma}_{Mc}$ given by a bad cosmology-redshift-mass-concentration fitting formula.

In a simplistic approach, the quadrature sum of the scatter coming from non-NFWness ($\sigma_{M-M(c)}$), the theoretical scatter (σ_{theo}) and the scatter due to a bad Mc fit ($\tilde{\sigma}_{Mc}$), should all add up to the scatter in the mass-mass conversion using a mass-concentration relation. Namely

$$\sigma^2_{M-M(Mc)} = \sigma^2_{M-M(c)} + \sigma^2_{theo} + \tilde{\sigma}^2_{Mc}. \tag{14}$$

5.4 Comparison of M_{200c} given M_{500c} or M_{2500c}

We study the case of converting masses M_{200c} given M_{500c} using techniques in Sec 5.2 and Sec 5.1.

The uncertainties, expressed as the logarithm of the ration between M_{200c} of C8 haloes obtained are as follows:

$$\begin{aligned} \sigma_{M-M} &= \quad 0.07 \\ \sigma_{M-M(Mc)} &= \quad 0.09 \\ \sigma_{M-M(c)} &= \quad 0.04 \\ \sigma_{theo} &= \quad 0.07 \\ \sqrt{\sigma^2_{M-M(c)} + \sigma^2_{theo}} &= \quad 0.09, \end{aligned} \tag{15}$$

where scatter σ_{M-M} is obtained using the mass-mass fit as Sec 5.2, the scatter $\sigma_{M-M(Mc)}$ is obtained using the Mc relation as Sec 5.1, the scatter $\sigma_{M-M(c)}$ is obtained using the true NFW concentration of each halo, and the scatter σ_{theo} is obtained using the law of error propagation as in Eq. 12. The quadrature sum of $\sigma_{M-M(c)}$ and σ_{theo} provides an estimate of the final scatter $\sigma_{M-M(Mc)}$ when considering non-NFWness as a only source of uncertainty.

We can see that, the mass conversion obtained with both the mass and concentration at a different overdensity is the one that gives the lowest scatter (i.e. column $\sigma_{M-M(c)}$). In other words, perfectly knowing the concentration of a cluster provides the less uncertain way to convert masses at different overdensities. In case one have only the mass at the original overdensity, the direct fit between halo masses is the one giving the lowest scatter (i.e. column σ_{M-M}).

The scatter $\sigma_{M-M(c)}$ accounts for $\approx 4\%$ for all haloes in all of our simulations. The quadrature sum of the theoretical scatter and $\sigma_{M-M(c)}$ is slightly lower than $\sigma_{M-M(Mc)}$. This implies that there is an additional source of scatter, although very small, probably coming from a non-ideal cosmology-redshift-mass-concentration fit (as in Table 2).

We do the same experiment as the one in our previous subsection, and we convert M_{2500} to M_{200}. Here below we show the residuals, expressed as the logarithm of the ration

[3] The package `hydro_mc` contains a sample script to convert masses between two overdensities by using the mass-concentration relation presented in this paper (http://github.com/aragagnin/hydro_mc/blob/master/examples/sample_mm_from_mc_relation.py).

Table 3. Fit parameters for Eq. 13 and Eq. 8 for overdensities $\Delta_{vir}, \Delta_{200c}, \Delta_{500c}, \Delta_{2500c}$ and Δ_{200m}. Pivots are as in Table 2. Errors on A_0, B_0, C_0 and σ are omitted as they are all $< 0.001\%$. The package `hydro_mc` contains a script that utilises this relation (`http://github.com/aragagnin/hydro_mc/blob/master/examples/sample_mm.py`).

Param	From overdensity → to overdensity					
	$vir \to 200c$	$vir \to 500c$	$vir \to 2500c$	$200c \to vir$	$200c \to 500c$	$200c \to 2500c$
$M_p[M_\odot]$	$1.99e+14$	$1.99e+14$	$1.99e+14$	$1.74e+14$	$1.74e+14$	$1.74e+14$
a_p	0.877	0.877	0.877	0.877	0.877	0.877
A_0	32.7166	32.314	31.340	32.989	32.393	31.413
B_0	1.00	0.996	0.925	0.995	0.994	0.922
C_0	-0.243	-0.237	-0.005	0.233	0.003	0.225
α_m	0.166 ± 0.007	0.29 ± 0.01	0.62 ± 0.03	-0.156 ± 0.006	0.125 ± 0.009	0.46 ± 0.02
α_b	0.00 ± 0.01	-0.02 ± 0.03	-0.16 ± 0.07	-0.003 ± 0.009	-0.02 ± 0.02	-0.15 ± 0.06
α_σ	0.048 ± 0.008	0.18 ± 0.02	0.57 ± 0.02	-0.036 ± 0.007	0.120 ± 0.008	0.54 ± 0.02
α_h	-0.045 ± 0.006	-0.10 ± 0.02	-0.05 ± 0.07	0.037 ± 0.004	-0.06 ± 0.01	-0.04 ± 0.06
β_m	-0.0166 ± 0.0004	-0.0424 ± 0.0003	-0.0758 ± 0.0007	0.0152 ± 0.0003	-0.0256 ± 0.0004	-0.0585 ± 0.0005
β_b	0.033 ± 0.002	0.095 ± 0.002	0.203 ± 0.004	-0.026 ± 0.001	0.068 ± 0.003	0.171 ± 0.003
β_σ	-0.024 ± 0.001	-0.043 ± 0.002	-0.010 ± 0.003	0.017 ± 0.001	-0.016 ± 0.002	0.006 ± 0.002
β_h	-0.010 ± 0.004	-0.038 ± 0.006	-0.203 ± 0.009	0.014 ± 0.005	-0.039 ± 0.007	-0.180 ± 0.009
γ_m	0.160 ± 0.001	0.213 ± 0.001	0.379 ± 0.001	-0.153 ± 0.001	0.053 ± 0.002	0.211 ± 0.002
γ_b	-0.055 ± 0.006	-0.113 ± 0.009	-0.232 ± 0.006	0.057 ± 0.006	-0.061 ± 0.009	-0.08 ± 0.01
γ_σ	0.119 ± 0.005	0.348 ± 0.006	0.555 ± 0.009	-0.110 ± 0.005	0.243 ± 0.007	0.486 ± 0.005
γ_h	0.05 ± 0.02	0.05 ± 0.02	0.04 ± 0.04	-0.03 ± 0.02	-0.02 ± 0.02	-0.18 ± 0.03
σ	0.0645	0.157845	0.3156	0.0748	0.1129	0.29619

Param	From overdensity → to overdensity					
	$500c \to vir$	$500c \to 200c$	$500c \to 2500c$	$2500c \to vir$	$2500c \to 200c$	$200c \to 500c$
$M_p[M_\odot]$	$1.37e+14$	$1.37e+14$	$1.37e+14$	$6.87e+13$	$6.87e+13$	$6.87e+13$
a_p	0.877	0.877	0.877	0.877	0.877	0.877
A_0	33.123	32.930	31.5754	33.3325	33.140	32.773
B_0	0.993	1.000	0.932	1.0201	1.027	1.031
C_0	0.252	0.017	0.219	0.1564	-0.078	-0.100
α_m	-0.26 ± 0.01	-0.114 ± 0.007	0.34 ± 0.01	-0.56 ± 0.03	-0.41 ± 0.02	-0.31 ± 0.01
α_b	0.00 ± 0.03	0.01 ± 0.02	-0.12 ± 0.05	0.1 ± 0.1	0.1 ± 0.1	0.09 ± 0.09
α_σ	-0.11 ± 0.01	-0.088 ± 0.009	0.41 ± 0.02	-0.34 ± 0.01	-0.32 ± 0.02	-0.26 ± 0.02
α_h	0.08 ± 0.03	0.06 ± 0.02	0.01 ± 0.08	0.1 ± 0.2	0.1 ± 0.2	0.0 ± 0.2
β_m	0.0339 ± 0.0004	0.0187 ± 0.0005	-0.0327 ± 0.0003	0.063 ± 0.001	0.0491 ± 0.0004	0.0289 ± 0.0003
β_b	-0.080 ± 0.002	-0.052 ± 0.003	0.115 ± 0.003	-0.30 ± 0.01	-0.264 ± 0.003	-0.189 ± 0.003
β_σ	0.035 ± 0.002	0.020 ± 0.002	0.031 ± 0.002	-0.019 ± 0.006	-0.035 ± 0.002	-0.045 ± 0.001
β_h	0.056 ± 0.007	0.039 ± 0.007	-0.199 ± 0.008	0.41 ± 0.03	0.38 ± 0.01	0.320 ± 0.006
γ_m	-0.191 ± 0.002	-0.036 ± 0.001	0.160 ± 0.001	-0.306 ± 0.001	-0.158 ± 0.002	-0.134 ± 0.002
γ_b	0.11 ± 0.01	0.028 ± 0.008	-0.068 ± 0.005	0.15 ± 0.01	0.07 ± 0.02	0.047 ± 0.010
γ_σ	-0.375 ± 0.008	-0.267 ± 0.006	0.228 ± 0.005	-0.64 ± 0.01	-0.535 ± 0.008	-0.268 ± 0.006
γ_h	-0.03 ± 0.03	0.05 ± 0.02	-0.11 ± 0.02	0.04 ± 0.06	0.15 ± 0.03	0.04 ± 0.02
σ	0.1291	0.0960	0.2340	0.2420	0.2272	0.1817

between the value of M_{200c} and M_{2500c}, when converting halo masses of the reference cosmology C8:

$$\begin{aligned} \sigma_{M-M} &= \quad 0.22 \\ \sigma_{M-M(Mc)} &= \quad 0.29 \\ \sigma_{M-M(c)} &= \quad 0.06 \\ \sigma_{theo} &= \quad 0.24 \\ \sqrt{\sigma^2_{M-M(c)} + \sigma^2_{theo}} &= \quad 0.25, \end{aligned} \tag{16}$$

The main difference with the M_{500} conversion is that in this case column σ_{theo} has a larger value than σ_{M-M} fit. Also, the scatter produced by converting masses using the Mc relation is less precise than the one using a direct mass-mass fit is the same. This implies that to convert from M_{2500} to M_{200} it is better to use the direct M-M fit proposed in Section 5.2.

6 DISCUSSIONS AND CONCLUSIONS

We computed concentrations and masses for a set of our simulations spanning 15 different cosmologies as in Table 1. We studied the concentration of our haloes in the critical overdensities $\Delta_{vir}, \Delta_{200c}, \Delta_{500c}, \Delta_{2500c}$ and mean overdensity Δ_{200m}. We showed how, in the context of hydrodynamic cosmological simulations, the mass-concentration plane is affected by the underlying cosmology and baryon physics. The logarithmic slope of mass dependency can go from positive to negative, although, given the large scatter in the mass-concentration relation (≈ 0.38), the role played by the mass concentration slope is minor, at least on cluster

Table 4. Fit parameters for Eq. 13 and Eq. 8 between overdensities of Δ_{200c} to Δ_{200m}. Errors on A_0, B_0, C_0 and σ are omitted as they are all $< 0.001\%$. Pivots are as in Table 2. The package `hydro_mc` contains a script that utilises this relation (`http://github.com/aragagnin/hydro_mc/blob/master/examples/sample_mm.py`).

Param	From overdensity $\rightarrow$ to overdensity $200c \rightarrow 200m$	$200m \rightarrow 200c$
$M_p[M_\odot]$	$1.74e+14$	$2.24e+14$
a_p	0.877	0.877
A_0	33.106	32.709
B_0	0.988	1.008
C_0	0.458	-0.492
α_m	-0.29 ± 0.01	0.32 ± 0.02
α_b	-0.02 ± 0.01	0.01 ± 0.02
α_σ	-0.05 ± 0.01	0.09 ± 0.02
α_h	0.078 ± 0.009	-0.103 ± 0.003
β_m	0.0306 ± 0.0004	-0.0351 ± 0.0005
β_b	-0.040 ± 0.003	0.063 ± 0.003
β_σ	0.029 ± 0.002	-0.050 ± 0.002
β_h	0.017 ± 0.006	-0.011 ± 0.007
γ_m	-0.313 ± 0.002	0.358 ± 0.002
γ_b	0.062 ± 0.008	-0.102 ± 0.010
γ_σ	-0.201 ± 0.007	0.246 ± 0.010
γ_h	0.03 ± 0.02	0.03 ± 0.04
σ	0.0830	0.1054

masses regime. Redshift dependency can vary up to a factor 3, and imply a larger effect in the evolution of concentration of haloes.

6.1 On the mass-concentration relation

The variation of mass-concentration plane in different simulations made it interesting to provide fit of the cosmology-redshift-mass-concentration relation for cosmological hydrodynamic simulations.

We did model the normalisation, the mass and redshift log-slope as a function of cosmology (see Eq. 8 and Eq. 6) and presented the results in Table 2. Figure 5 (upper panels) shows the normalisation of the mass-concentration relation is nearly independent from h_0, is slightly pushed down by Ω_b ($\alpha_b \approx -0.2$) in case of $\Delta = 2500c$, furthermore concentration is typically pushed up almost equally by Ω_m and σ_8 ($\alpha_m, \alpha_\sigma \approx 0.5$).

The logarithmic slope of the mass is leaded by Ω_m and Ω_b, and they have contribute with opposite signs: being $\alpha_m < 0$, then a larger Ω_m makes the log-slope smaller, and being $\alpha_b > 0$, a larger Ω_b makes the mass log-slope larger. There is also a secondary effect of σ_8, whole related coefficient (β_σ) is typically half of α_b and α_m.

For the highest overdensity Δ_{2500c}, the Hubble parameter h_0 (with the corresponding $\beta_h = -0.34$) plays a strong role in decreasing the mass log-slope. Being the Δ_{2500c} regime mainly influenced by radiative, stellar, and black hole physics. The dependency from h_0 may be due to these scale-dependent processes, which are acting on time scales decoupled from the background evolution.

6.2 On the direct mass-mass fit

In order to study the conversion of masses between two overdensities Δ_1 and Δ_2, we provided a fit of the mass $M_{\Delta 2}$ as a function of $M_{\Delta 1}$, redshift and cosmological parameters. We did model these dependencies in a similar way to the mass concentration relation (see Eq. 13), where the normalisation, mass and redshift log-slopes depends on cosmological parameters as in Eq. 8.

We present our mass-mass relation in Table 3, Table 4 and Figure 5 (bottom panels). This relation is useful because it convert masses without imposing a NFW hypothesis on the density profile. The normalisation is mainly affected by Ω_m and σ_8 parameters (see α_m and α_s respectively).

When converting masses from higher overdensities to lower overdensities, their scatter increases as the difference between overdensities increases. When converting $\Delta_1 \rightarrow \Delta_2$, with $\Delta_1 > \Delta_2$ (e.g. $\Delta_{500c} \rightarrow \Delta_{200c}$), the parameters α_m and α_s are positive (i.e. the higher Ω_m and σ_8, the higher the normalisation) and has a scatter of ≈ 0.1. When converting back or forth to Δ_{2500c}, the parameter Ω_b (i.e. α_b is not negligible) starts playing a role in the normalisation, (although the $\alpha_b \approx 0.1$ is still lower than α_m and α_m) in particular, the higher Ω_b, the lower the normalisation.

The log-slope of the mass dependency (β parameters) has almost no dependency from cosmology and has a value of $B_0 \approx 1$. One exception is made when converting from/to Δ_{2500c}, where the slope depends on h_0 (with a positive correlation) and Ω_b (with a negative correlation). This means that sparsity typically does not depends on mass.

The redshift dependence (γ parameters) is mostly influenced by Ω_m and σ_8, with a contribution that increases the higher is the separation between overdensities, for instance when converting $\Delta_{2500c} \rightarrow \Delta_{vir}$ on has $\gamma_m \approx 0.4$ $\gamma_\sigma \approx 0.6$. These values mean that the higher Ω_m and σ_8, the higher the growth of mass ratio with redshift.

Figure 5. Evolution of concentration (top panel) from the fit parameters in Table 2) and sparsity parameter (bottom panel) from the fit in Table 3 as a function of cosmological parameters $(\Omega_m, \Omega_b, \sigma_8, h_0)$ centred in the values of the reference cosmology C8 $(\Omega_m = 0.272, \Omega_b = 0.0456, \sigma_8 = 0.809, h_0 = 0.704)$.

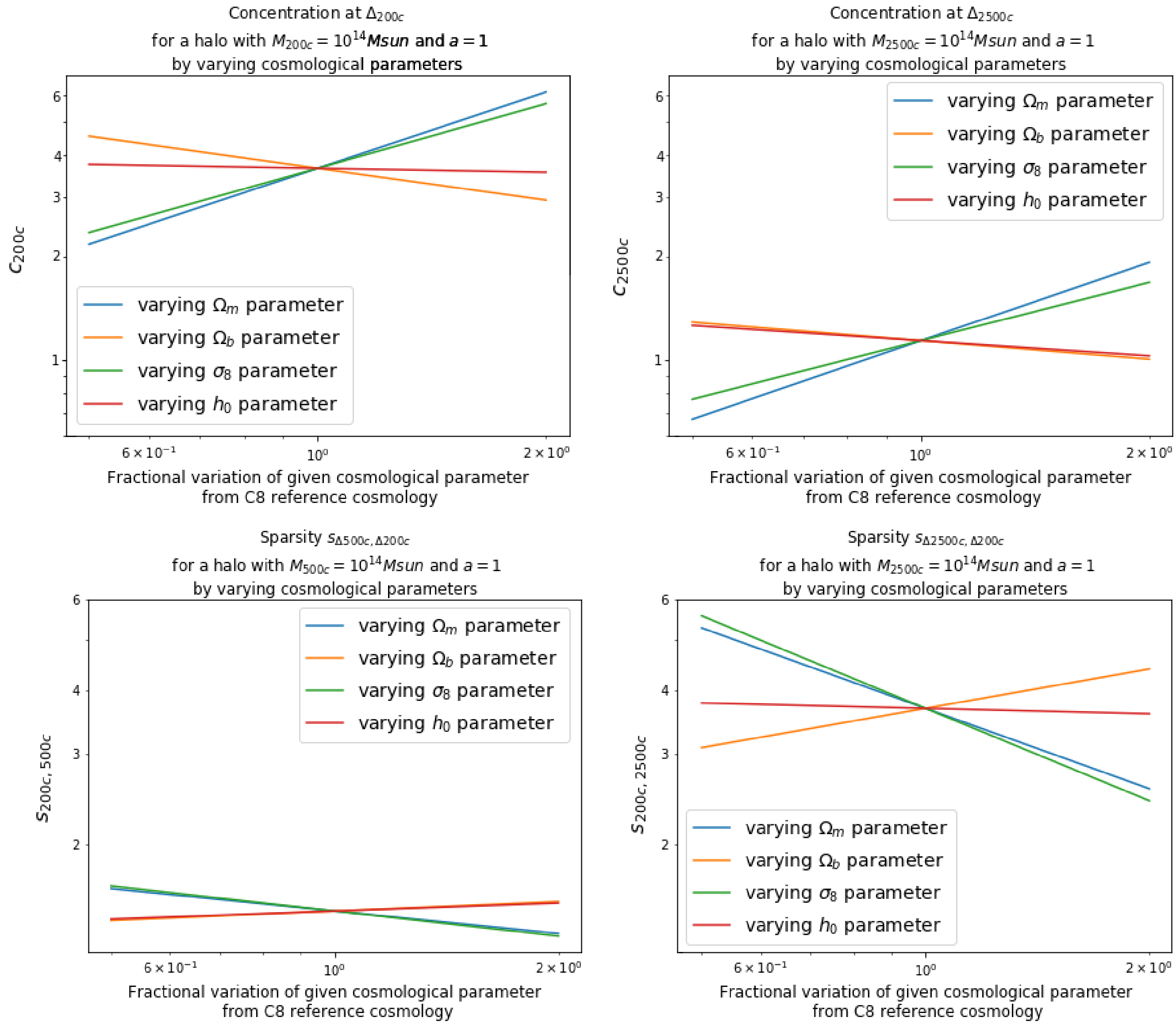

6.3 On the uncertainty of the mass-mass convertions

We studied the possibility of using the Mc relation as a proxy to convert masses from one overdensity to another.

Part of the scatter in the mass-mass conversion performed with a Mc relation comes from the non-NFWness of profiles (approx. $0.05 - 0.07$ of the scatter). For the M_{2500} to M_{200} conversion, a fractional scatter of ≈ 0.15 is given by the inability of the Mc relation fit to perfectly capture the dependency between M_{2500}, z and cosmology on c_{2500}, or even the assumption of a log-normal distribution of values.

The picture changes dramatically when trying to convert M_{2500} to M_{200}. Albeit being the intrinsic scatter of this relationship higher ($\sigma \approx 0.25$), the cosmology-mass-mass fit predicts much better the final mass.

6.4 Final remarks

Simulations as $C1$ and $C2$ have positive correlation between mass and concentration. This is in agreement with Prada et al. (2012), where they found that haloes with low σ (as given by the low σ_8 of of C1 and C2) have a concentration that increases with mass. Additionally, this behaviour is supposed to be due to a non-NFWness of dark matter profiles with very low σ (see Section 3.5 in Prada et al. 2012).

In general, for this kind of conversion, we suggest to use a direct cosmology-mass-mass conversion as in Table 3 and Table 4, this is not based on assuming a NFW density profile.

We released the python package `hydro_mc` (github.com/aragagnin/hydro_mc). This tool able to perform all kind of conversions presented in this paper and we provided a number of ready to use examples: mass-concentration relation presented in Table 2 (`http://github.com/aragagnin/hydro_mc/blob/master/examples/sample_mc.py`), mass-mass conversion with fit parameters in Table 3 (`http://github.com/aragagnin/hydro_mc/blob/master/examples/sample_mm.py`), and mass-mass conversion through the Mc relation in Table 2 (`http://github.com/aragagnin/hydro_mc/blob/master/examples/sample_mm_from_mc_relation.py`).

Given the wide different mass-concentration planes one can obtain by an incorrect baryon physics (i.e. the adiabatic run '_norad'), and by varying the concentration, more work is needed to follow the evolution of the same haloes in different simulations to understand in which way cosmological parameters and baryon physics change concentration.

ACKNOWLEDGEMENTS

The *Magneticum Pathfinder* simulations were partially performed at the Leibniz-Rechenzentrum with CPU time assigned to the Project 'pr86re'. This work was supported by the Deutsche Forschungsgemeinschaft (DFG, German Research Foundation) under Germany's Excellence Strategy - EXC-2094 - 390783311. AR is supported by the EuroEXA project (grant no. 754337). KD acknowledges support by DAAD contract number 57396842. AR acknowledges support by MIUR-DAAD contract number 34843 „The Universe in a Box". AS and PS are supported by the ERC-StG 'ClustersXCosmo' grant agreement 716762. AS is supported by the the FARE-MIUR grant 'ClustersXEuclid' R165SBKTMA. We are especially grateful for the support by M. Petkova through the Computational Center for Particle and Astrophysics (C^2PAP). Information on the *Magneticum Pathfinder* project is available at `http://www.magneticum.org`.

REFERENCES

Achitouv I., Baldi M., Puchwein E., Weller J., 2016, Phys. Rev. D, 93, 103522
Andreon S., Moretti A., Trinchieri G., Ishwara-Chand ra C. H., 2019, A&A, 630, A78
Balmès I., Rasera Y., Corasaniti P. S., Alimi J. M., 2014, MNRAS, 437, 2328
Bartalucci I., Arnaud M., Pratt G. W., Démoclès J., Lovisari L., 2019, A&A, 628, A86
Beck A. M., et al., 2016, MNRAS, 455, 2110
Becker M. R., Kravtsov A. V., 2011, ApJ, 740, 25
Bellstedt S., et al., 2018, MNRAS, 476, 4543
Bhattacharya S., Habib S., Heitmann K., Vikhlinin A., 2013, ApJ, 766, 32
Biffi V., Dolag K., Böhringer H., 2013, MNRAS, 428, 1395
Biviano A., Girardi M., 2003, ApJ, 585, 205
Biviano A., et al., 2013, A&A, 558, A1
Biviano A., et al., 2017, A&A, 607, A81
Bocquet S., Saro A., Dolag K., Mohr J. J., 2016, MNRAS, 456, 2361
Bocquet S., et al., 2019, ApJ, 878, 55
Boylan-Kolchin M., Springel V., White S. D. M., Jenkins A., Lemson G., 2009, MNRAS, 398, 1150
Brainerd T., 2019, in American Astronomical Society Meeting Abstracts #233. p. 338.06
Bulbul E., et al., 2019, ApJ, 871, 50
Bullock J. S., Kolatt T. S., Sigad Y., Somerville R. S., Kravtsov A. V., Klypin A. A., Primack J. R., Dekel A., 2001, MNRAS, 321, 559
Buote D. A., Barth A. J., 2019, ApJ, 877, 91
Capasso R., et al., 2019, arXiv e-prints, p. arXiv:1910.04773
Ciesielski K., 2007, Banach J. Math. Anal., 1, 1
Corasaniti P. S., Rasera Y., 2019, MNRAS, 487, 4382
Corasaniti P. S., Ettori S., Rasera Y., Sereno M., Amodeo S., Breton M. A., Ghirardini V., Eckert D., 2018, ApJ, 862, 40
Corsini E. M., et al., 2018, A&A, 618, A172
De Boni C., 2013, arXiv e-prints,
De Boni C., Ettori S., Dolag K., Moscardini L., 2013, MNRAS, 428, 2921
Diemer B., Joyce M., 2019, ApJ, 871, 168
Diemer B., Kravtsov A. V., 2015, ApJ, 799, 108
Dietrich J. P., et al., 2019, MNRAS, 483, 2871
Dodelson S., 2003, Modern cosmology
Dolag K., Bartelmann M., Perrotta F., Baccigalupi C., Moscardini L., Meneghetti M., Tormen G., 2004, A&A, 416, 853
Dolag K., Borgani S., Murante G., Springel V., 2009, MNRAS, 399, 497
Dolag K., Gaensler B. M., Beck A. M., Beck M. C., 2015, MNRAS, 451, 4277
Dolag K., Komatsu E., Sunyaev R., 2016, MNRAS, 463, 1797
Duffy A. R., Schaye J., Kay S. T., Dalla Vecchia C., Battye R. A., Booth C. M., 2010, MNRAS, 405, 2161
Fabjan D., Borgani S., Tornatore L., Saro A., Murante G., Dolag K., 2010, MNRAS, 401, 1670
Ferland G. J., Korista K. T., Verner D. A., Ferguson J. W., Kingdon J. B., Verner E. M., 1998, PASP, 110, 761
Foreman-Mackey D., Hogg D. W., Lang D., Goodman J., 2013, PASP, 125, 306
Frenk C. S., et al., 1999, ApJ, 525, 554
Fujita Y., Umetsu K., Rasia E., Meneghetti M., Donahue M., Medezinski E., Okabe N., Postman M., 2018a, ApJ, 857, 118
Fujita Y., Umetsu K., Ettori S., Rasia E., Okabe N., Meneghetti M., 2018b, ApJ, 863, 37
Fujita Y., et al., 2019, Galaxies, 7, 8
Ghigna S., Moore B., Governato F., Lake G., Quinn T., Stadel J., 1998, MNRAS, 300, 146
Gupta N., Saro A., Mohr J. J., Dolag K., Liu J., 2017, MNRAS, 469, 3069
Heitmann K., et al., 2016, ApJ, 820, 108
Hirschmann M., Dolag K., Saro A., Bachmann L., Borgani S., Burkert A., 2014, MNRAS, 442, 2304
Hu W., Kravtsov A. V., 2003, ApJ, 584, 702
Kendall E., Easther R., 2019, arXiv e-prints, p. arXiv:1908.02508
Klypin A. A., Trujillo-Gomez S., Primack J., 2011, ApJ, 740, 102
Klypin A., Yepes G., Gottlöber S., Prada F., Heß S., 2016, MNRAS, 457, 4340
Komatsu E., et al., 2009, ApJS, 180, 330
Komatsu E., et al., 2011, ApJS, 192, 18
Kravtsov A. V., Klypin A. A., Khokhlov A. M., 1997, ApJS, 111, 73
Kwan J., Bhattacharya S., Heitmann K., Habib S., 2013, ApJ, 768, 123
Lin W. P., Jing Y. P., Mao S., Gao L., McCarthy I. G., 2006, ApJ, 651, 636
Ludlow A. D., Navarro J. F., Angulo R. E., Boylan-Kolchin M., Springel V., Frenk C., White S. D. M., 2014, MNRAS, 441, 378
Macciò A. V., Dutton A. A., van den Bosch F. C., 2008, MNRAS, 391, 1940
Mamon G. A., Biviano A., Boué G., 2013, MNRAS, 429, 3079
Mandelbaum R., Seljak U., Hirata C. M., 2008, J. Cosmology Astropart. Phys., 8, 006
Mantz A. B., 2019, MNRAS, 485, 4863
Martinsson T. P. K., Verheijen M. A. W., Westfall K. B., Ber-

shady M. A., Andersen D. R., Swaters R. A., 2013, A&A, 557, A131
McClintock T., et al., 2019, MNRAS, 482, 1352
Meneghetti M., et al., 2014, ApJ, 797, 34
Merten J., et al., 2015, ApJ, 806, 4
Navarro J. F., Frenk C. S., White S. D. M., 1996, ApJ, 462, 563
Navarro J. F., Frenk C. S., White S. D. M., 1997, ApJ, 490, 493
Okoli C., 2017, arXiv e-prints, p. arXiv:1711.05277
Prada F., Klypin A. A., Cuesta A. J., Betancort-Rijo J. E., Primack J., 2012, MNRAS, 423, 3018
Pratt G. W., Pointecouteau E., Arnaud M., van der Burg R. F. J., 2016, A&A, 590, L1
Ragagnin A., Tchipev N., Bader M., Dolag K., Hammer N. J., 2016, in Advances in Parallel Computing, Volume 27: Parallel Computing: On the Road to Exascale, Edited by Gerhard R. Joubert, Hugh Leather, Mark Parsons, Frans Peters, Mark Sawyer. IOP Ebook, ISBN: 978-1-61499-621-7, pages 411-420. (arXiv:1810.09898), doi:10.3233/978-1-61499-621-7-411
Ragagnin A., Dolag K., Moscardini L., Biviano A., D'Onofrio M., 2019, MNRAS, 486, 4001
Remus R.-S., Dolag K., 2016, in The Interplay between Local and Global Processes in Galaxies,. p. 43
Remus R.-S., Dolag K., Naab T., Burkert A., Hirschmann M., Hoffmann T. L., Johansson P. H., 2017, MNRAS, 464, 3742
Rey M. P., Pontzen A., Saintonge A., 2018, arXiv e-prints,
Roos M., 2003, Introduction to Cosmology, Third Edition
Saro A., et al., 2014, MNRAS, 440, 2610
Schulze F., Remus R.-S., Dolag K., Burkert A., Emsellem E., van de Ven G., 2018, MNRAS, 480, 4636
Shan H., et al., 2017, ApJ, 840, 104
Shirasaki M., Lau E. T., Nagai D., 2018, MNRAS, 477, 2804
Singh P., Saro A., Costanzi M., Dolag K., 2019, arXiv e-prints, p. arXiv:1911.05751
Spergel D. N., et al., 2003, ApJS, 148, 175
Spergel D. N., et al., 2007, ApJS, 170, 377
Springel V., 2005, MNRAS, 364, 1105
Springel V., White S. D. M., Tormen G., Kauffmann G., 2001, MNRAS, 328, 726
Springel V., Di Matteo T., Hernquist L., 2005a, MNRAS, 361, 776
Springel V., et al., 2005b, Nature, 435, 629
Steinborn L. K., Dolag K., Hirschmann M., Prieto M. A., Remus R.-S., 2015, MNRAS, 448, 1504
Steinborn L. K., Dolag K., Comerford J. M., Hirschmann M., Remus R.-S., Teklu A. F., 2016, MNRAS, 458, 1013
Suto Y., 2003, arXiv e-prints, pp astro–ph/0311575
Teklu A. F., Remus R.-S., Dolag K., Beck A. M., Burkert A., Schmidt A. S., Schulze F., Steinborn L. K., 2015, ApJ, 812, 29
Teklu A. F., Remus R.-S., Dolag K., 2016, in The Interplay between Local and Global Processes in Galaxies,. p. 41
Tollet E., et al., 2016, MNRAS, 456, 3542
Tornatore L., Borgani S., Dolag K., Matteucci F., 2007, Monthly Notices of the Royal Astronomical Society, 382, 1050
Umetsu K., et al., 2019, arXiv e-prints, p. arXiv:1909.10524
Wang L., Dutton A. A., Stinson G. S., Macciò A. V., Penzo C., Kang X., Keller B. W., Wadsley J., 2015, MNRAS, 454, 83
van de Sande J., et al., 2019, MNRAS, 484, 869

APPENDIX A: COSMOLOGY-MASS-REDSHIFT-CONCENTRATION RELATION LITE

Given the weak dependency of mass from the concentration (at least in the mass range of interests of cluster of galaxies), we provide a cosmology-redshift-mass-concentration fit where, in Eq. 6 we parametrise the dependency of the cosmology only in the normalisation and in the redshift dependency as the following:

$$\begin{aligned}
A &= A_0 + \alpha_m \ln\left(\frac{\Omega_m}{\Omega_{m,p}}\right) + \alpha_b \ln\left(\frac{\Omega_b}{\Omega_{b,p}}\right) + \\
&\quad + \alpha_\sigma \ln\left(\frac{\sigma_8}{\sigma_{8,p}}\right) + \alpha_h \ln\left(\frac{h_0}{h_{0,p}}\right) \\
B &= B_0 \qquad\qquad / \qquad\qquad\qquad (\mathrm{A1}) \\
C &= C_0 + \gamma_m \ln\left(\frac{\Omega_m}{\Omega_{m,p}}\right) + \gamma_b \ln\left(\frac{\Omega_b}{\Omega_{b,p}}\right) + \\
&\quad + \gamma_\sigma \ln\left(\frac{\sigma_8}{\sigma_{8,p}}\right) + \gamma_h \ln\left(\frac{h_0}{h_{0,p}}\right)
\end{aligned}$$

Table A1 show the results of this fit, with the same procedure as in Section 4, where pivot values are the ones for thre reference cosmology C8 and errors are assigned by performing the same fit as in Singh et al. (2019).

Table A2 show the results of the mass-concentration plane where we fit the NFW profile of the dark matter density profile only. The functional form is as in Eq. A1, with the same procedure as the previous one (thus, as in Section 4).

APPENDIX B: THEORETICAL SCATTER OF MASS CONVERSION USING AN MC RELATION

Equation system 11 shows how the concentration in an overdensity Δ_2 is uniquely identified by the concentration in Δ_1 by solving bottom equation in Eq. 11. Although there are four variables in Eq. 11 (namely $M_{\Delta 1}$, $M_{\Delta 2}$, $c_{\Delta 1}$ and $c_{\Delta 2}$), since there are two equations the system depends on two of them.

Hu & Kravtsov (2003) provides a fitting formula for $c_{\Delta 2}$ as a function of $c_{\Delta 1}$. On the other hand since $c_{\Delta 2}$ depends monotonically from right side of Eq. 11, in this work we convert the values from $c_{\Delta 1}$ to $c_{\Delta 2}$ using the fixed-point technique derived by solving equation 11 the Banach-Cacioppoli theorem (see e.g. Ciesielski 2007, for a review).

To evaluate $c_{\Delta 2}$ we start with a guess value of $c_{\Delta 1}$ and iteratively apply it to Eq. 11 in order to get the new value of value of $c_{\Delta 2}$, until it converges, practically we fix $\frac{\Delta_1}{\Delta_2}$ and $c_{\Delta,1}$ rewrite Eq. 11 as

$$\begin{aligned}
\tilde{c}\,(x) &\equiv \quad c_{\Delta 1} \cdot \left(\frac{\Delta_1}{\Delta_2}\frac{f(x)}{f(c_{\Delta 1})}\right)^{\frac{1}{3}} \qquad (\mathrm{B1}) \\
c_{\Delta 2} &= \qquad \tilde{c}\,(c_{\Delta 2})\,.
\end{aligned}$$

We found that the relative error after 9 iterations is, at the worst, comparable with Hu & Kravtsov (2003) and can go down to 10^{-9} for concentration values higher than 20. As a first value we choose $c_{\Delta 1}$, so

$$c_{\Delta 2} \approx \tilde{c}\,(\tilde{c}\,(\tilde{c}\,(\tilde{c}\,(\tilde{c}\,(\tilde{c}\,(\tilde{c}\,(\tilde{c}\,(\tilde{c}\,(c_{\Delta 1}))))))))) \qquad (\mathrm{B2})$$

Figure B1 shows the relative error when converting M_{500c} and M_{2500c} to M_{200c}. Both approach have an error smaller than $\approx 0.1\%$, while the iteration proposed here can reach much more precise value and it is easier to implement.

Table A1. Pivots and fit parameters for the cosmology dependent redshift-mass-concentration plane as Table 2, here the logarithmic slope of mass is not dependent on cosmology, thus we fit Eq. 6 and Eq. A1, for concentration overdensities of $\Delta = \Delta_{\tt vir}, \Delta_{200c}, \Delta_{500c}, \Delta_{2500c}$ and Δ_{200m}. The pivots $\Omega_{m,p}, \Omega_{b,p}, \sigma_8$ and h_0 in Eq. 8 are the cosmological parameters of C8 as in Table 1 ($\Omega_m = 0.272, \Omega_b = 0.0456, \sigma_8 = 0.809, h_0 = 0.704$). Errors on A_0, B_0, C_0 and σ are omitted as they are all $< 0.001\%$. The package `hydro_mc` contains a script that utilises this relation (http://github.com/aragagnin/hydro_mc/blob/master/examples/sample_mc_lite.py).

Parameter	Overdensity				
	vir	200c	500c	2500c	200m
$M_p[M_\odot]$	$1.99e+14$	$1.74e+14$	$1.37e+14$	$6.87e+13$	$2.24e+14$
a_p	0.877	0.877	0.877	0.877	0.877
A_0	1.499	1.238	0.859	0.122	1.688
B_0	-0.048	-0.053	-0.060	-0.037	-0.044
C_0	0.520	0.201	0.187	0.110	0.910
α_m	0.423 ± 0.006	0.60 ± 0.01	0.63 ± 0.01	0.7273 ± 0.0006	0.201 ± 0.003
α_b	-0.141 ± 0.006	-0.152 ± 0.006	-0.131 ± 0.005	-0.179 ± 0.004	-0.186 ± 0.006
α_σ	0.65 ± 0.02	0.65 ± 0.02	0.61 ± 0.03	0.516 ± 0.003	0.60 ± 0.02
α_h	-0.28 ± 0.01	-0.25 ± 0.02	-0.27 ± 0.02	-0.23 ± 0.01	-0.17 ± 0.02
γ_m	0.19 ± 0.01	0.360 ± 0.010	0.336 ± 0.009	0.36 ± 0.01	-0.10 ± 0.01
γ_b	0.02 ± 0.06	-0.15 ± 0.06	-0.04 ± 0.05	0.00 ± 0.07	0.00 ± 0.06
γ_σ	0.76 ± 0.05	0.72 ± 0.04	0.89 ± 0.04	0.94 ± 0.06	0.61 ± 0.05
γ_h	-0.4 ± 0.2	-0.1 ± 0.2	-0.4 ± 0.2	-0.5 ± 0.2	-0.4 ± 0.2
σ	0.388031	0.384516	0.376690	0.382868	0.388477

[ht]

Table A2. Fit parameters for the cosmology dependent redshift-mass-concentration plane as Table 2, here we computed the concentration using the scale radius of the dark matter density profile, plus the logarithmic slope of mass is not dependent on cosmology. We fit Eq. 6 and Eq. A1, for concentration overdensities of $\Delta = \Delta_{\tt vir}, \Delta_{200c}, \Delta_{500c}, \Delta_{2500c}$ and Δ_{200m}. The pivots $\Omega_{m,p}, \Omega_{b,p}, \sigma_8$ and h_0 in Eq. 8 are the cosmological parameters of C8 as in Table 1 ($\Omega_m = 0.272, \Omega_b = 0.0456, \sigma_8 = 0.809, h_0 = 0.704$). Errors on A_0, B_0, C_0 and σ are omitted as they are all $< 0.001\%$. The package `hydro_mc` contains a script that utilises this relation (http://github.com/aragagnin/hydro_mc/blob/master/examples/sample_mc_dm_lite.py).

Parameter	Overdensity				
	vir	200c	500c	2500c	200m
A_0	1.499	1.238	0.979	0.213	1.798
B_0	-0.048	-0.053	-0.039	-0.015	-0.034
C_0	0.520	0.201	0.178	0.055	0.918
α_m	0.42 ± 0.05	0.60 ± 0.01	0.46 ± 0.07	0.588 ± 0.001	0.008 ± 0.007
α_b	-0.14 ± 0.03	-0.152 ± 0.006	-0.08 ± 0.03	-0.204 ± 0.010	-0.072 ± 0.006
α_σ	0.65 ± 0.03	0.65 ± 0.02	0.47 ± 0.05	0.363 ± 0.006	0.53 ± 0.01
α_h	-0.28 ± 0.05	-0.25 ± 0.02	-0.33 ± 0.05	-0.47 ± 0.03	0.03 ± 0.01
γ_m	0.19 ± 0.04	0.360 ± 0.010	0.34 ± 0.01	0.51 ± 0.03	-0.23 ± 0.01
γ_b	0.02 ± 0.06	-0.15 ± 0.06	-0.4 ± 0.1	-0.7 ± 0.1	-0.09 ± 0.06
γ_σ	0.76 ± 0.06	0.72 ± 0.04	0.5 ± 0.1	0.3 ± 0.1	0.45 ± 0.02
γ_h	-0.4 ± 0.2	-0.1 ± 0.2	-1.1 ± 0.4	-1.9 ± 0.5	0.02 ± 0.06
σ	0.39	0.384516	0.51	0.484290	0.498887

Only 9 iterations produce a relative error that in the worst case is comparable with technique in Hu & Kravtsov (2003) and it is capable of going down to 10^{-8}.

Figure B2 show the convsersion from overdensities $\Delta_2 = 2500$ and $\Delta_2 = 500$ to $\Delta_1 = 200$. These relations are nearly linear with a deviation for lower concentrations.

Another interesting property of Eq. 11 is the possibility of knowing $M_{\Delta 2}/M_{\Delta 1}$ only by knowing $c_{\Delta 1}$.

Figure B3 shows such conversions for overdensitites Δ_{2500c} and Δ_{500c} to $\Delta_{200c}1$. This conversion gets flatter and flatter as the concentration increases, implying that the higher the concentration the lower the error one makes in this conversion.

It is possible to estimate this uncertainty analytically. Given the fact that Mc relations are nown with uncertainties, it is interesting to see how to propagate the error analitically when converting from $c_{\Delta 1}$ to $c_{\Delta 2}$, which is proportional to the derivarive caming from Eq. 9:

$$\frac{dc_{\Delta 2}}{dc_{\Delta 1}} = \frac{c_{\Delta 2}}{c_{\Delta 1}} + \frac{1}{3}\frac{c_{\Delta 2}}{f\left(c_{\Delta 1}\right)}\left.\frac{df(c)}{dc}\right|_{c=c_{\Delta 1}}\frac{dc_{\Delta 2}}{dc_{\Delta 1}} - \\ -\frac{1}{3}\frac{c_{\Delta 2}}{f\left(c_{\Delta 1}\right)}\left.\frac{df(c)}{dc}\right|_{c=c_{\Delta 2}}, \tag{B3}$$

where $f(c)$ is, in case of imposing a NFW profile, given in Eq. 10. One can rearrange Eq. B3 to isolate the derivative:

$$\frac{dc_{\Delta 2}}{dc_{\Delta 1}} = \frac{\frac{c_{\Delta 2}}{c_{\Delta 1}} - \frac{1}{3}\frac{c_{\Delta 2}}{f\left(c_{\Delta 1}\right)}\left.\frac{df(c)}{dc}\right|_{c=c\Delta 2}}{1 - \frac{1}{3}\frac{c_{\Delta 2}}{f\left(c_{\Delta 1}\right)}\left.\frac{df(c)}{dc}\right|_{c=c\Delta 1}} \tag{B4}$$

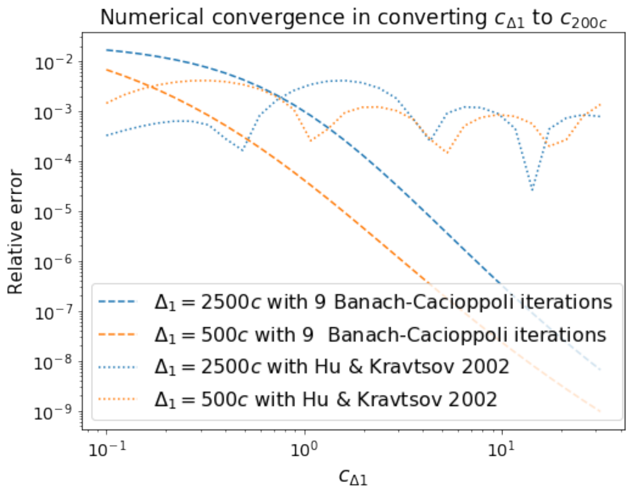

Figure B1. Relative error when converting the concentration using Eq. B1 (i.e. Banach-Cacioppoli theorem) or using the method proposed in Hu & Kravtsov (2003)

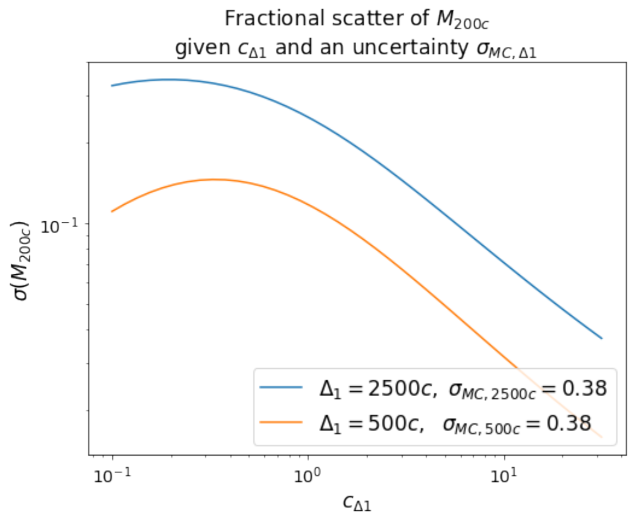

Figure B2. Analytical uncertainty on the concentration obtained by the theoretical propagation of error

One can understand how a uncertainty propagates analytically from $M_{\Delta 2}\left(M_{\Delta 1}, c_{\Delta 1}\right)$ in Eq. 11, by computing the derivative

$$\frac{dM_{\Delta 2}}{dc_{\Delta 1}} = \frac{\partial M_{\Delta 2}}{\partial c_{\Delta 1}} + \frac{\partial M_{\Delta 2}}{\partial M_{\Delta 1}} \frac{dM_{\Delta 1}}{dc_{\Delta 1}},$$

given the very weak dependency of mass from concentration, we can approximate

$$\frac{dM_{\Delta 1}}{dc_{\Delta 1}} \approx 0,$$

one gets

$$\frac{dM_{\Delta 2}}{dc_{\Delta 1}} = 3M_{\Delta 2}\left(\frac{1}{c_{\Delta 2}}\frac{dc_{\Delta 2}}{dc_{\Delta 1}} - \frac{1}{c_{\Delta 1}}\right),$$

where $dc_{\Delta 2}/dc_{\Delta 1}$ is evaluated as in Eq. B4.

Figure B4 show the uncertainty variation when converting to M_{200} for a scatter in the concentration compatible

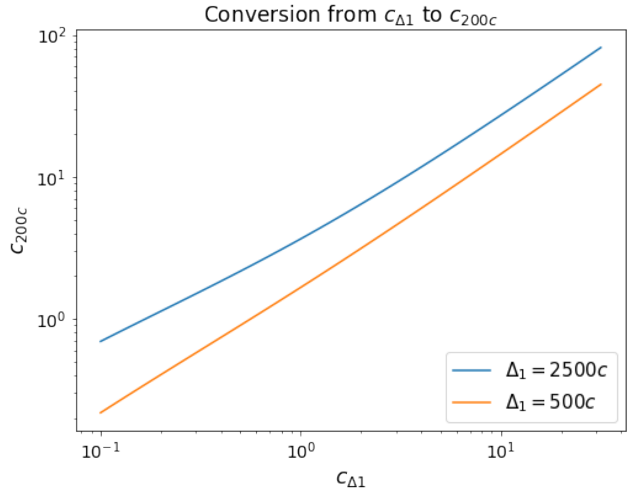

Figure B3. Analytical value of c_{200c} for a given concentration $c_{\Delta 1}$. We used $\Delta 1 = 500c$ and $\Delta 1 = 2500c$.

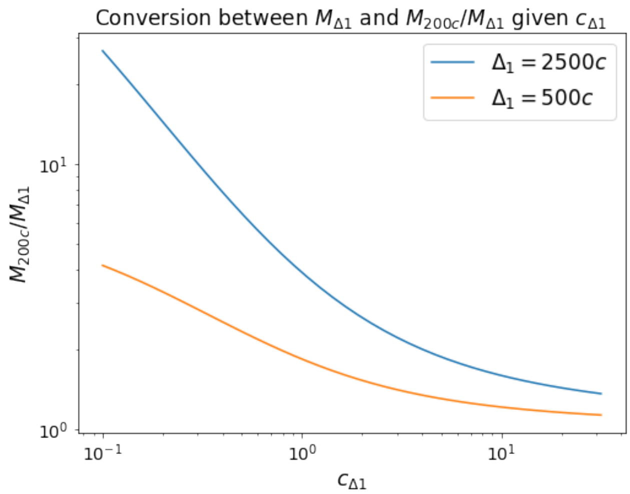

Figure B4. Analytical value of M_{200c} with respect to $M_{\Delta 1}$ for a given concentration $c_{\Delta 1}$. We used $\Delta 1 = 500c$ and $\Delta 1 = 2500c$.

with the scatter wefound in our Mc relation (see Table 2). This is helpful in understanding the actualy scatter one find in real case scenarios as Sections 5.2 and 5.1.

This paper has been typeset from a TEX/LATEX file prepared by the author.